

A millimeter-sized nanomanipulator with sub-nanometer positioning resolution and large force output

This article has been downloaded from IOPscience. Please scroll down to see the full text article.

2007 Smart Mater. Struct. 16 1742

(<http://iopscience.iop.org/0964-1726/16/5/029>)

View [the table of contents for this issue](#), or go to the [journal homepage](#) for more

Download details:

IP Address: 128.100.48.213

The article was downloaded on 07/10/2010 at 23:18

Please note that [terms and conditions apply](#).

A millimeter-sized nanomanipulator with sub-nanometer positioning resolution and large force output

Xinyu Liu, Jianhua Tong and Yu Sun¹

Department of Mechanical and Industrial Engineering, University of Toronto,
5 King's College Road, Toronto, ON, M5S 3G8, Canada

E-mail: sun@mie.utoronto.ca

Received 3 April 2007, in final form 17 July 2007

Published 22 August 2007

Online at stacks.iop.org/SMS/16/1742

Abstract

Nanomanipulation in space-limited environments (e.g., inside a SEM (scanning electron microscope), and particularly in a TEM (transmission electron microscope)) requires small-sized nanomanipulators that are capable of producing sub-nanometer positioning resolutions and large output forces. This paper reports on a millimeter-sized MEMS (microelectromechanical systems) based nanomanipulator with a positioning resolution of 0.15 nm and a motion range of $\pm 2.55 \mu\text{m}$. An amplification mechanism is employed to convert micrometer input displacements, generated by a conventional electrostatic comb-drive microactuator, into sub-nanometer output displacements. The device has a high load driving capability, driving a load as high as $98 \mu\text{N}$ without sacrificing positioning performance. Based on the pseudo-rigid-body approach, closed-form analytical models of the minification ratio and stiffness of the amplification mechanism are developed. Finite element simulation and testing results verify that the theoretical models are valid with an error smaller than 6.2% and that the mechanism has a high linearity ($\pm 2.4\%$). The amplification mechanism and analytical models have general applicability to other MEMS transducer designs. A capacitive displacement sensor is integrated for detecting input displacements that are converted into output displacements via the minification ratio, allowing closed-loop controlled nanomanipulation. The MEMS-based nanomanipulators are applicable to the characterization/manipulation of nanomaterials and construction of nanodevices.

(Some figures in this article are in colour only in the electronic version)

1. Introduction

Recent advances in nanoscience and nanotechnology, including the manipulation and characterization of nanomaterials (e.g., carbon nanotubes, silicon nanowires and zinc oxide nanorods) and NEMS (nanoelectromechanical systems) development, require millimeter-sized manipulators with sub-nanometer positioning resolutions, micrometer motion ranges, high repeatability and large output forces.

Existing nanomanipulators with electron-discharge-machined stages and piezoelectric actuators can achieve a resolution of 1 nm [1, 2]. However, inherent hysteresis and creep of piezoelectric actuators result in significant open-loop positioning errors, and therefore demand sophisticated compensation control algorithms [2, 3]. Besides the high cost, the large sizes of commercially available piezoelectric nanomanipulators (5–10 cm) limit their use when applications have stringent space restrictions (e.g., inside SEM and TEM) [4, 5].

MEMS microactuators have been employed in nanopositioning applications due to their low cost, small size, fast

¹ Author to whom any correspondence should be addressed.

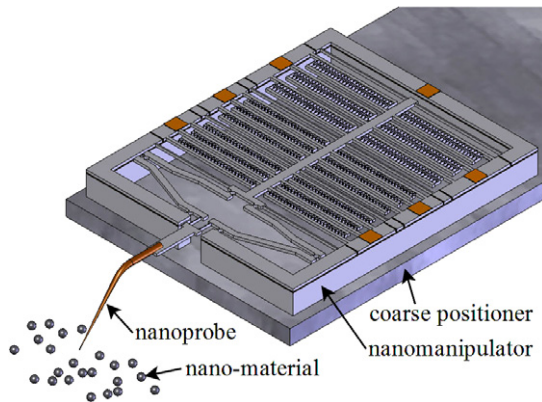


Figure 1. Millimeter-sized MEMS nanomanipulator with a motion range of micrometers and resolution of sub-nanometers for precisely manipulating nanometer-sized objects.

response and flexibility for system integration. In particular, electrostatic microactuators are most commonly used for nanopositioning. Traditional electrostatic microactuators are capable of providing typical resolutions of the order of 10 nm [6–8]. Compared to other microactuation mechanisms (e.g., electrothermal and electromagnetic), electrostatic microactuation offers the fastest response and the best repeatability that is critical for applications at the nanoscale. However, the small output force capability of electrostatic microactuators limits their practical applications in the manipulation of nano-objects.

A recently reported electrostatic surface drive actuator [9] demonstrates a better positioning resolution (0.05 nm) than traditional electrostatic actuators. However, when nanometer/sub-nanometer output displacements are produced by microstepping, the stepping actuation principle inherently decreases output forces dramatically, which makes the design unsuitable for nanomanipulation use. Additionally, the device requires complex actuation and sensing circuitries that are not commercially available; therefore, significant efforts need to be spent on circuit design and on-chip integration.

Electrothermal microactuators were also employed in the development of nanopositioners [10]. Although electrothermal microactuation provides much larger output forces, hysteresis and thermal drift make the positioning accuracy relative low

(hundreds of nanometers). Furthermore, the difficulty of well-controlled temperatures at the probe tip prevents its use in temperature-sensitive applications.

This paper presents the design, fabrication and testing of a millimeter-sized nanomanipulator that leverages the high repeatability and fast response of MEMS electrostatic microactuators while overcoming the limitation of low output forces. The device integrates a highly linear amplification mechanism, a lateral comb-drive microactuator and a capacitive displacement sensor. The amplification mechanism is used to minify input displacements for achieving a high positioning resolution at the output probe tip and to amplify output forces for manipulating nano-objects. Figure 1 shows a conceptual schematic where the MEMS-based millimeter-sized nanomanipulator is used to manipulate nanospheres.

2. Nanomanipulator working principle

The nanomanipulator shown in figure 2 consists of a linear amplification mechanism, a lateral comb-drive microactuator and a capacitive displacement sensor. The linear amplification mechanism is used to convert large input motion (μm) into small output motion (nm), enormously enhancing the positioning resolution. The comb-drive actuator consisting of groups of interdigitated comb fingers produces bi-directional motion that is resolved by the capacitive displacement sensor. The measurement of input displacements enables closed-loop position control of the comb-drive actuator. A central input shaft connects the amplification mechanism, lateral comb-drive actuator and capacitive displacement sensor. The structures are suspended by eight straight supporting beams.

Amplification mechanisms are widely used in traditional piezoelectric nanopositioning stages [11, 12] and MEMS transducer designs [13–15] to amplify output displacements. The amplification of output displacements unavoidably requires that input actuation forces be very large to overcome the large input stiffness. Meanwhile, output forces decrease with the same ratio as displacement amplification. Amplified motion and reduced output force are not desired in nanomanipulation, which requires high motion resolution, high repeatability and large output forces.

The design reported in this paper employs a linear amplification mechanism to operate in a minification mode,

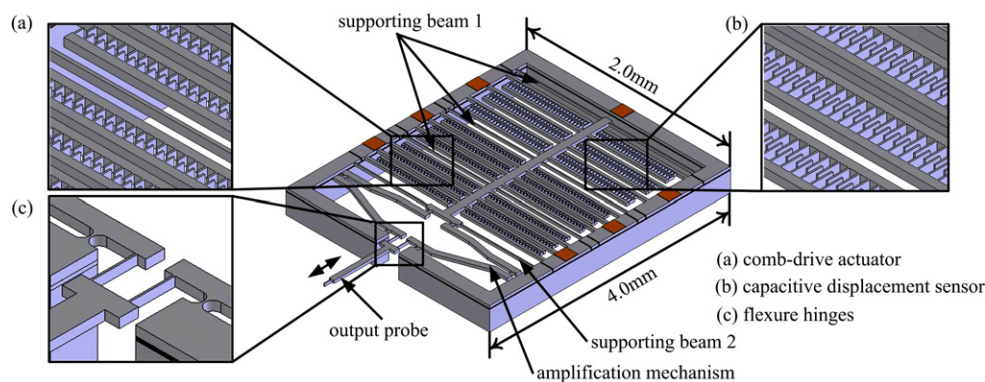


Figure 2. Solid model of the MEMS nanomanipulator with capacitive displacement sensor.

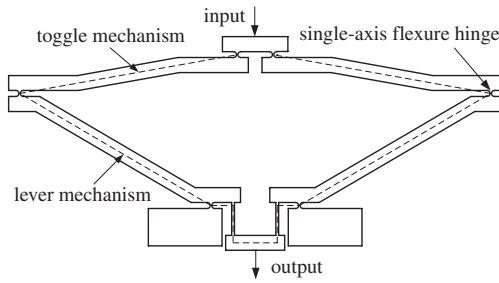


Figure 3. Schematics of inverse-mode linear amplification mechanism.

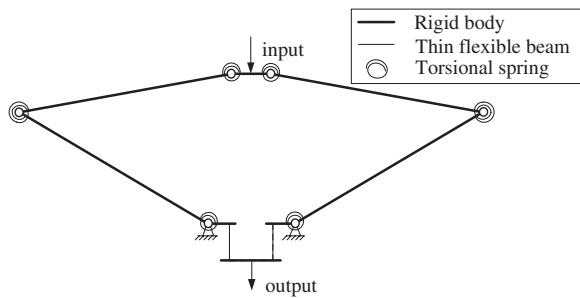


Figure 4. Pseudo-rigid-body model of the linear amplification mechanism.

shown in figure 3, in order to minify input displacements and amplify output forces. The mechanism integrates two typical amplification mechanisms: toggle mechanism and lever mechanism, which are connected in series by single-axis flexure hinges. The input displacement is minified by the toggle mechanism first, and then the lever mechanism decreases the motion further. In order to eliminate lateral displacements at the output end caused by lever rotation, two pairs of toggle mechanisms and lever mechanisms are symmetrically configured. Two thin flexible beams connect the two output ends of the lever mechanisms and the output platform in order to avoid lateral motion (figures 2(c) and 3). This two-stage amplification configuration was recently demonstrated to operate in the amplification mode in a macro-scaled piezoelectric stage design [12]. Compared to the two-stage lever amplification mechanism [16], the employment of a toggle mechanism makes a toggle-lever amplification mechanism producing a higher displacement amplification ratio with a more compact structure [12, 17].

It is well known that electrostatic microactuators have fast response, but low force output. In this design, the input stiffness of the amplification mechanism was designed to be sufficiently low such that comb-drive microactuators on the input side are capable of driving the amplification mechanism to generate large forward and backward motions. To precisely measure input displacements, a capacitive displacement sensor is integrated at the input end as a position encoder. As the experimental results show, the amplification mechanism is highly linear. Thus, the capacitive displacement feedback on the input side can be used to reliably predict displacements on the output side. The position feedback enables precise closed-loop control of nanopositioning during nanomanipulation.

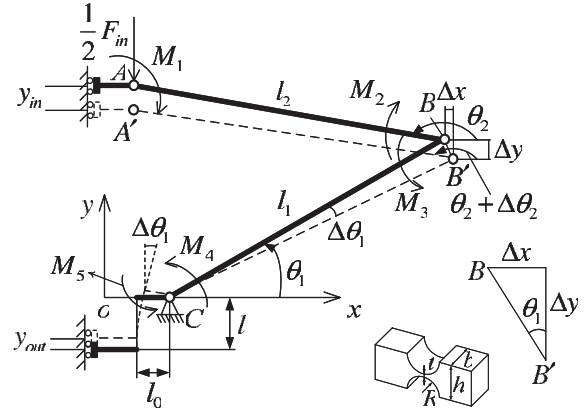


Figure 5. Displacement and stiffness analysis.

3. Device design

3.1. Amplification mechanism structure design

In order to provide a systematic design approach for determining structural parameters of the amplification mechanism, an analytical model based on the pseudo-rigid-body approach [18] is developed. The flexure hinge (figure 3) is treated as a rotational joint and a torsional spring that connect two rigid bodies (figure 4).

3.1.1. Minification ratio. The minification ratio is determined by analyzing displacement transmission of the mechanism. Due to symmetry, only half of the mechanism with equivalent boundary conditions is described in figure 5.

An input displacement y_{in} driven by the electrostatic actuator is minimized by the toggle mechanism first and produces small position offsets at point B in both x and y directions (i.e., Δx and Δy). The lever mechanism conducts the second-stage displacement minification and minifies the displacement of point B to the final output displacement y_{out} .

To achieve strictly linear behavior, the lengths of the rigid bars are set much larger than the input displacement ($l_1, l_2 \gg y_{in}$) so that the angle changes ($\Delta\theta_1$ and $\Delta\theta_2$) can be treated as infinitesimals. Thus, the amplification ratio of the toggle mechanism is

$$\alpha_t = \cot \theta_2. \tag{1}$$

Consequently, the first-stage minification is

$$y_{in} = \Delta x \cot \theta_2 + \Delta y. \tag{2}$$

Because $\Delta\theta_1$ is infinitesimal, BB' is considered perpendicular to BC and, consequently, the angle between BB' and the y axis can be approximated by θ_1 . Therefore, the following two equations hold:

$$\Delta x = -\tan \theta_1 \Delta y \tag{3}$$

$$\Delta \theta_1 = \frac{\overline{BB'}}{l_1} = \frac{\Delta y}{l_1 \cos \theta_1}. \tag{4}$$

Combining equations (2) and (3) yields

$$\Delta y = \frac{y_{in}}{1 - \tan \theta_1 \cot \theta_2}. \tag{5}$$

The final output displacement is

$$y_{\text{out}} = -l_0 \Delta\theta_1. \quad (6)$$

Substituting equations (4), (5) and (6) yields the total displacement minification ratio

$$\alpha = \frac{y_{\text{out}}}{y_{\text{in}}} = -\frac{l_0}{l_1(\cos\theta_1 - \sin\theta_1 \cot\theta_2)} \quad (7)$$

where the minus sign represents opposite directions of y_{in} and y_{out} .

3.1.2. Stiffness analysis. A closed-form static stiffness model of the amplification mechanism is derived based on the pseudo-rigid-body model. The Paros and Weisbord equation [19] is used to estimate the stiffness of the equivalent torsional spring

$$K_{\text{hinge}} = \frac{2Ebt^{5/2}}{9\pi R^{1/2}} \quad (8)$$

where E is the Young's modulus of silicon, and b , t and R are specified in figure 5. In this design, all hinges have the same dimensional parameters.

When a force F_{in} is applied, the equivalent force in the analytical model is half of F_{in} . This force causes an angle change between rigid bars. Thus, the flexure hinges and thin flexible beams generate reaction torques, as illustrated in figure 5. These reaction torques are

$$M_1 = -K_{\text{hinge}} \Delta\theta_2 \quad (9)$$

$$M_2 = -M_3 = K_{\text{hinge}} (\Delta\theta_1 - \Delta\theta_2) \quad (10)$$

$$M_4 = -K_{\text{hinge}} \Delta\theta_1. \quad (11)$$

Considering the boundary conditions at the output end, the bending model of fixed-free beams [20] can be used to estimate the reaction torque generated by the thin flexible beams, which can be expressed as

$$M_5 = -\frac{Ewh^3}{12l} \Delta\theta_1 \quad (12)$$

where w , h and l are width, height and length of the thin flexible beams.

Through a static analysis of the lever mechanism, the following torque equilibrium equation is obtained:

$$\frac{1}{2} F_{\text{in}} l_1 \cos\theta_1 + M_3 + M_4 + M_5 = 0. \quad (13)$$

Substituting equations (10), (11), and (12) into (13) yields

$$\frac{1}{2} F_{\text{in}} l_1 \cos\theta_1 + K_{\text{hinge}} \Delta\theta_2 - \left(\frac{Ewh^3}{12l} + 2K_{\text{hinge}} \right) \Delta\theta_1 = 0. \quad (14)$$

From figure 5, trigonometry gives

$$\sin(\theta_2 + \Delta\theta_2) = \frac{l_2 \sin\theta_2 - \Delta\theta_1 l_1 \sin\theta_1 \cot\theta_2 - l_1 \cos\theta_1 \Delta\theta_1}{l_2} \quad (15)$$

$$\cos(\theta_2 + \Delta\theta_2) = \frac{l_2 \cos\theta_2 - l_1 \Delta\theta_1 \sin\theta_1}{l_2}. \quad (16)$$

Because $\Delta\theta_2$ can be treated as infinitesimal, it can be approximated as

$$\begin{aligned} \Delta\theta_2 &= \sin\Delta\theta_2 \\ &= \sin(\theta_2 + \Delta\theta_2) \cos\theta_2 - \cos(\theta_2 + \Delta\theta_2) \sin\theta_2 \\ &= -\frac{l_1}{l_2} [\cos(\theta_1 + \theta_2) + \sin\theta_1 \cos\theta_2 \cot\theta_2] \Delta\theta_1. \end{aligned} \quad (17)$$

Substituting equations (6), (7), and (17) into (14) yields

$$\begin{aligned} F_{\text{in}} &= \frac{2\alpha}{l_0 l_1 \cos\theta_1} \left\{ -\frac{l_1}{l_2} K_{\text{hinge}} [\cos(\theta_1 + \theta_2) \right. \\ &\quad \left. + \sin\theta_1 \cos\theta_2 \cot\theta_2] - 2K_{\text{hinge}} - \frac{Ewh^3}{12l} \right\} y_{\text{in}}. \end{aligned} \quad (18)$$

Thus, the input stiffness of the amplification mechanism is

$$\begin{aligned} K_{\text{mechanism}} &= \frac{2\alpha}{l_0 l_1 \cos\theta_1} \left\{ -\frac{l_1}{l_2} K_{\text{hinge}} [\cos(\theta_1 + \theta_2) \right. \\ &\quad \left. + \sin\theta_1 \cos\theta_2 \cot\theta_2] - 2K_{\text{hinge}} - \frac{Ewh^3}{12l} \right\}. \end{aligned} \quad (19)$$

Taking into account the stiffness of the other eight flexible beams supporting the input shaft (figure 2), the total input stiffness of the device is

$$\begin{aligned} K_{\text{sum}} &= \frac{2\alpha}{l_0 l_1 \cos\theta_1} \left\{ -\frac{l_1}{l_2} K_{\text{hinge}} [\cos(\theta_1 + \theta_2) \right. \\ &\quad \left. + \sin\theta_1 \cos\theta_2 \cot\theta_2] - 2K_{\text{hinge}} - \frac{Ewh^3}{12l} \right\} \\ &\quad + \frac{6EW_1 H_1^3}{L_1^3} + \frac{2EW_2 H_2^3}{L_2^3} \end{aligned} \quad (20)$$

where W_1 , H_1 and L_1 are width, height and length of supporting beam 1; and W_2 , H_2 , and L_2 are width, height and length of supporting beam 2 (figure 2).

3.2. Actuation and position sensing design

3.2.1. Actuator design. A lateral comb-drive actuator is chosen to drive the nanomanipulator. As shown in figure 2, the actuator consists of two groups of comb fingers that generate forward and backward input displacements and thus drive the output probe back and forth. The total electrostatic force is

$$F_e = \frac{1}{2} \frac{N_a \epsilon h_f}{g} V^2 \quad (21)$$

where $\epsilon = 8.85 \times 10^{-12} \text{ C}^2 \text{ N}^{-1} \text{ m}^{-2}$ is the permittivity of air, V the actuation voltage, h_f the finger thickness, g the gap between adjacent comb fingers and N_a is the number of actuation comb finger pairs. Therefore, the output displacement is

$$y_{\text{out}} = \pm \frac{\alpha}{K_{\text{sum}}} F_e = \pm \frac{1}{2} \frac{\alpha}{K_{\text{sum}}} \frac{N_a \epsilon h_f}{g} V^2 \quad (22)$$

where the signs differentiate backward and forward motions.

3.2.2. Capacitive displacement sensor design. Figure 2(b) shows the lateral comb-drive displacement sensor. When the actuators generate an input displacement, the center input shaft carries the movable sensing comb fingers to move by the same displacement. Ignoring fringing capacitance, the total capacitance change is

$$\Delta C = \frac{N_s \epsilon h_f'}{g'} y_{\text{in}} \quad (23)$$

Table 1. Nanomanipulator design parameters.

Structural parameters	
Base	2.0 mm × 4.0 mm
Amplification mechanism	$l_0 = 75 \mu\text{m}$, $l_1 = 300 \mu\text{m}$, $l_2 = 300 \mu\text{m}$, $\theta_1 = 20^\circ$, $\theta_2 = 165^\circ$
Flexure hinge	$b = 10 \mu\text{m}$, $t = 2 \mu\text{m}$, $R = 8 \mu\text{m}$
Support beam 1	$W_1 = 8 \mu\text{m}$, $H_1 = 10 \mu\text{m}$, $L_1 = 780 \mu\text{m}$
Support beam 2	$W_2 = 8 \mu\text{m}$, $H_2 = 10 \mu\text{m}$, $L_2 = 820 \mu\text{m}$
Thin flexible beams	$w = 2 \mu\text{m}$, $h = 10 \mu\text{m}$, $l = 80 \mu\text{m}$
Actuation and sensing parameters	
Lateral comb actuator	$N_a = 4670$, $V_{\max} = 60 \text{ V}$, $h_f = 10 \mu\text{m}$, $g = 2 \mu\text{m}$
Displacement sensor	$N_s = 1092$, $h'_f = 10 \mu\text{m}$, $g' = 2 \mu\text{m}$

Table 2. Silicon material properties used in FEA.

Density	2.329 g cm ⁻³
Young's modulus	129.5 GPa
Poisson's ratio	0.28

Table 3. Theoretical and FEA results of device specifications.

	Theoretical	FEA	Difference (%)
Input stiffness ($\mu\text{N } \mu\text{m}^{-1}$)	16.80	16.84	0.24
Minification ratio	-0.1128	-0.1187	5.0

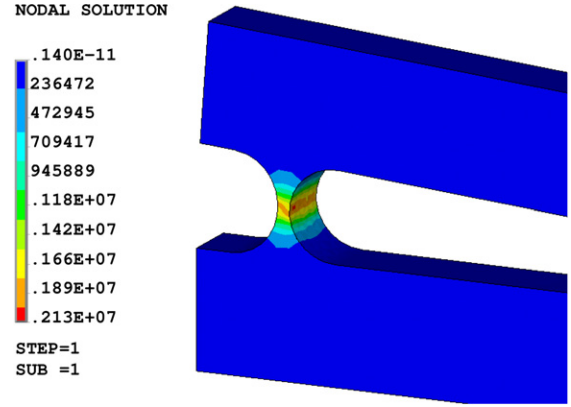
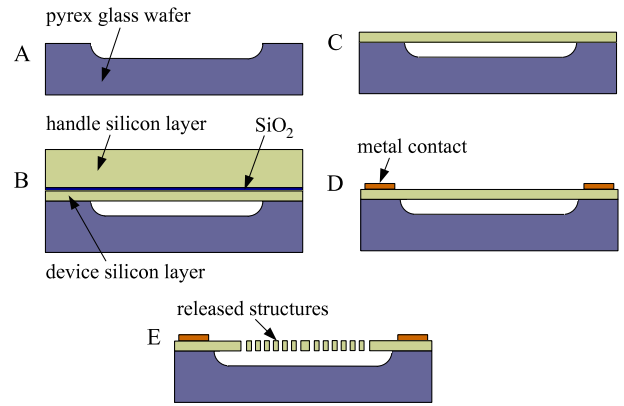
where h'_f and g' are both constants, denoting thickness and sensing gap distance; and N_s is the number of sensing comb finger pairs. Hence, input displacements y_{in} are resolved by measuring the total capacitive change, ΔC , of the capacitive displacement sensor. Due to the high linearity of the amplification mechanism, which will be discussed in section 5.1, the output displacement can also be accurately predicted via

$$y_{\text{out}} = \alpha y_{\text{in}} = \frac{\alpha g'}{N_s \epsilon h'_f} \Delta C. \quad (24)$$

3.2.3. Finite element simulation. The main design parameters of the nanomanipulator (i.e., amplification mechanism, comb-drive actuator and capacitive displacement sensor) are listed in table 1. Based on these parameters, finite element analysis (FEA) was conducted using ANSYS® to verify the validity of the developed theoretical models of the amplification mechanism and to analyze the performance of the nanomanipulator design. In simulation, 10-node Solid 92 tetrahedron elements were employed for meshing. Table 2 shows silicon material parameters used in the simulation.

Electrostatic actuation forces proportional to the input voltage squared were calculated according to equation (21). These actuation forces were then applied as input to the finite element model. The FEA results are summarized in table 3. The theoretical calculation results based on the derived closed-form models ((7), (19) and (20)) are in agreement with the FEA simulation results with errors within 5% in the complete output motion range ($\pm 2.55 \mu\text{m}$), proving the validity of the derived minification ratio and stiffness models.

Due to bending, maximum stress occurs at two flexure hinges connecting toggle mechanisms with lever mechanisms (figure 6). The maximum stress in the complete motion range

**Figure 6.** Stress distribution at one flexure hinge connecting toggle and lever mechanisms.**Figure 7.** Microfabrication process.

($\pm 2.55 \mu\text{m}$) was found to be within 2.1 GPa, which is well within the yield strength of silicon (7 GPa) [21].

As out-of-plane motion of the nanomanipulator probe tip is undesired, it was also investigated using FEA. The results show that out-of-plane displacements are within $\pm 1 \text{ nm}$ in the complete motion range ($\pm 2.55 \mu\text{m}$), confirming that the nanomanipulator has a satisfactory stability in the out-of-plane direction.

4. Device fabrication

The MEMS-based nanomanipulators were fabricated through a foundry process (Micalryne) with a glass wafer and a silicon-

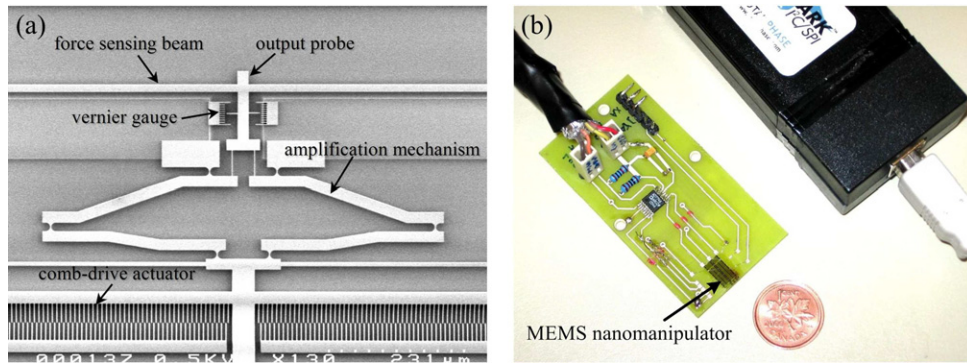


Figure 8. (a) SEM picture of a released device. (b) Nanomanipulator on a PCB that contains a capacitance readout circuit.

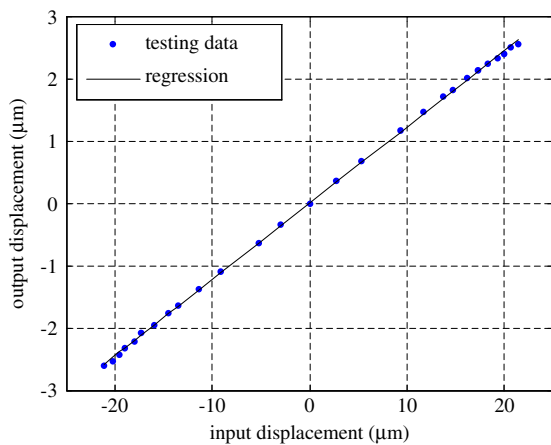


Figure 9. Experimental data of output versus input displacements.

on-insulator (SOI) wafer, using wet glass etching, wet silicon etching and silicon deep reactive ion etching (DRIE). The fabrication process, as illustrated in figure 7, is summarized as follows:

- Step A. The fabrication process begins with a $500 \pm 25 \mu\text{m}$ thick glass wafer, on which 12 μm deep cavities are etched using BOE etching.
- Step B. An SOI wafer is anodically bonded to the patterned glass wafer with the device layer (10 μm thick) facing down.
- Step C. The silicon handle layer and buried SiO_2 box layer are etched away, leaving only the single-crystal silicon device layer on top of the glass substrate.
- Step D. Metal layers of 500 \AA thick Ti-W and 2000 \AA Au are evaporated onto the device layer to form ohmic contacts, and are patterned using wet etching.
- Step E. The device layer is finally etched through using DRIE to form comb fingers, amplification mechanism and other features.

5. Testing results and discussion

Figure 8(a) shows a released MEMS nanomanipulator. A Vernier gauge at the output end is used for measuring output displacements. For device testing, it was glued and wire-bonded to a custom-made printed circuit board

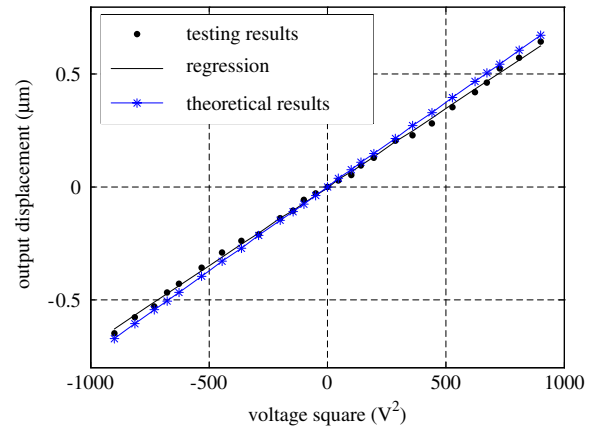


Figure 10. Experimental and theoretical results of output displacements versus actuation voltage squared.

(PCB) that contains a capacitance readout circuit, as shown in figure 8(b). A DC power supply (AMREL SPS600-2) was used for providing 0–60 V actuation voltages. Device characterization was conducted on a vibration isolation table, at room temperature and with minimal air flow.

5.1. Actuation characterization

The displacements at input and output ends of the amplification mechanism were measured using high-resolution optical imaging. A microscope with 100 \times objective (NA 0.42) and a commercial digital camera with an image size of 3264 \times 2448 pixels (Nikon Coolpix 8400, 3.5 \times optical lens) were used for measuring input and output motions. The pixel size was calibrated to be 32.26 nm/pixel. A sub-pixel autocorrelation algorithm [22] was used for tracking the movable features, and the tracking resolution is 0.08 pixel. Thus, the measurement resolution of input and output displacements is 2.58 nm with the optical measurement set-up.

Figure 9 shows the testing results of output displacements as a function of input displacements, proving a linearity of $\pm 2.4\%$ and a minification ratio of -0.1151 for the amplification mechanism. At 60 V, the nanomanipulator is capable of generating $\pm 2.55 \mu\text{m}$ output displacements. A 30 V voltage produces an output displacement of $\pm 650 \text{ nm}$ (figure 10). Compared to experimental data, the derived theoretical model of the amplification mechanism satisfactorily predicts output displacements with an error $\leq 6.2\%$.

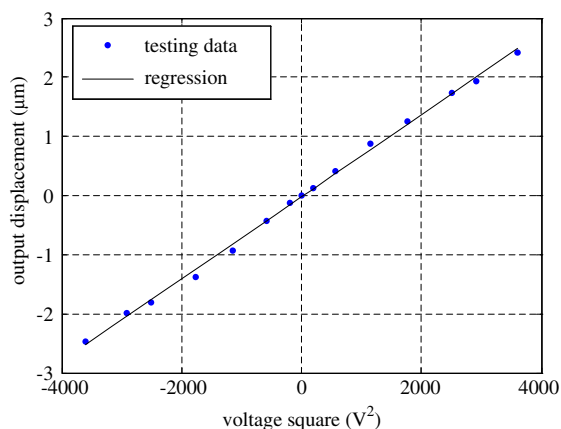


Figure 11. Testing results of output displacements with force sensing beams.

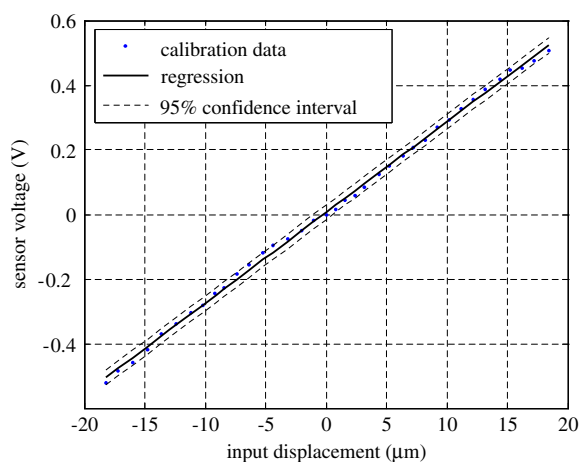


Figure 12. Calibration data of capacitive displacement sensor.

Two fixed-guided thin beams (figure 8(a)) are attached to the output probe for quantifying output forces of the nanomanipulator. The total stiffness of the force sensing beams is $40.5 \mu\text{N } \mu\text{m}^{-1}$. The measured output displacements with force sensing beams are shown in figure 11. The maximum output displacement is $\pm 2.42 \mu\text{m}$, corresponding to a maximum output force of $98 \mu\text{N}$. Compared to the zero-load case ($\pm 2.55 \mu\text{m}$), the maximum displacement is only reduced by 5.1%, demonstrating a strong load driving capability of the nanomanipulator.

5.2. Capacitive displacement sensing characterization

Capacitance changes of the displacement sensor were measured by a readout circuit based on an ASIC from Analog Devices (AD7746). AD7746 is capable of converting capacitance changes into voltage changes with high linearity ($\pm 0.01\%$). Figure 12 shows the calibration results of the capacitive displacement sensor, proving a linear relationship between voltage changes and input displacements. The resolution of the readout circuit was determined to be $30 \text{ aF } \text{Hz}^{-1/2}$ that corresponds to an input displacement resolution of 1.31 nm in a 10 Hz bandwidth. The integrated capacitive displace-

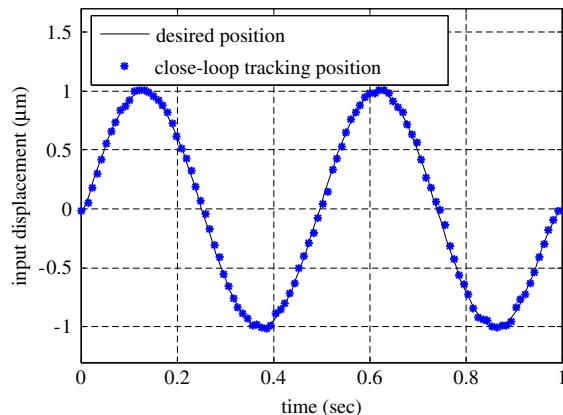


Figure 13. Experimental results of closed-loop sinusoidal tracking.

Table 4. Device specifications.

MEMS nanomanipulator	
Device size	2 mm × 4 mm
Output motion resolution	$0.15 \pm 0.0036 \text{ nm}$
Output displacement	$\pm 2.55 \mu\text{m}$
Actuation voltage	0–60 V
Position sensor resolution	1.31 nm
Output force	$98 \mu\text{N}$
Resonant frequency	3.1 kHz
Amplification mechanism	
Minification ratio	–0.1151
Linearity	$\pm 2.4\%$

ment sensor permits the execution of closed-loop controlled nanopositioning/nanomanipulation. Figure 13 shows the experimental results of closed-loop sinusoidal tracking using PID (proportional-integral-derivative) control.

Considering the high input–output linearity from the amplification mechanism (experimentally determined to be $\pm 2.4\%$), capacitive position feedback on the input side can be used to reliably predict minified output displacements. Thus, the output positioning resolution was determined by scaling the input resolution (1.31 nm) with the minification ratio (0.1151), which results in an output positioning resolution of $0.15 \pm 0.0036 \text{ nm}$ with the uncertainty arising from the $\pm 2.4\%$ linearity. Testing results of the MEMS nanomanipulator are summarized in table 4.

5.3. Discussion

When operating inside an SEM or TEM, charges from electron beams can disturb the capacitive position sensor of the MEMS nanomanipulators unless the capacitive sensor is electrically isolated from other structures that are exposed to electron beams for imaging. In order to achieve this purpose, a DRIE-SOI process [23] permits electrical isolation and mechanical connection, which would make the capacitive position sensors immune from disturbances by electron beams of SEM or TEM.

Thermal-mechanical noise-induced vibration is a factor that may impose a limitation on the position resolution of the nanomanipulators. In order to quantify this thermodynamic

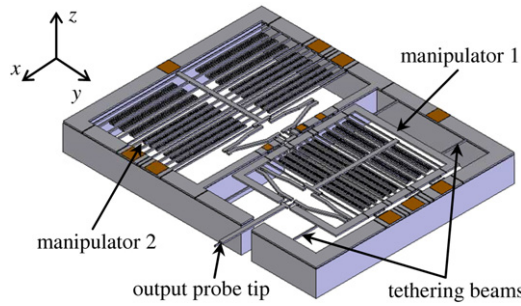


Figure 14. Solid model of a two-axis MEMS nanomanipulator.

vibration, Nyquist's relation [24] was employed for calculating the noise force

$$F = \sqrt{4k_B T D} \quad (25)$$

where k_B is Boltzmann's constant ($1.38 \times 10^{-23} \text{ J K}^{-1}$), T the absolute temperature and D the damping of the system. The damping D can be expressed by

$$D = \frac{\sqrt{Km}}{Q} \quad (26)$$

where K is the output stiffness, m the mass and Q the mechanical quality factor. For the nanomanipulator, $T = 298 \text{ K}$, $K = 141.9 \mu\text{N } \mu\text{m}^{-1}$ and $m = 1.04 \times 10^{-7} \text{ kg}$. Assuming typical values of 1–10 for Q , the noise force is calculated to be within $0.8 \times 10^{-11} \text{ N Hz}^{-1/2}$. Thus, vibration displacements at the output probe are

$$x_{\text{noise}} = \frac{F\sqrt{f}}{K} \quad (27)$$

where f is the resonant frequency of the device. The thermal-mechanical noise-induced displacement is thus calculated to be less than 0.0031 nm. This result indicates that thermal-mechanical noise is not a significant error source for sub-nanometer positioning with the MEMS nanomanipulator.

The millimeter-sized MEMS nanomanipulators provide many design flexibilities. For instance, it can be readily extended to two-axis nanomanipulators by orthogonally connecting two one-axis nanomanipulators in series, as shown in figure 14. Manipulator 1, responsible for driving the probe tip along the x direction, is suspended by four tethering beams. Manipulator 2 drives manipulator 1 to generate motion along the y direction. In addition, the closed-form analytical models of the amplification mechanism permit designers to readily adjust the position resolution and motion range without going through lengthy finite element simulations. The MEMS nanomanipulators also allow one to mount nanometer-sized end effectors on the manipulator probe for interacting with nanoscaled materials (figure 1).

6. Conclusion

This paper presented the design, fabrication and testing of a millimeter-sized MEMS nanomanipulator. The device has a positioning resolution of 0.15 nm, an output motion range of $\pm 2.55 \mu\text{m}$ and a high force output capability (i.e., outputting a force of $98 \mu\text{N}$ reduces motion range only by 5.1%).

An amplification mechanism operating in the minification mode with a high linearity ($\pm 2.4\%$) was employed to minify input displacements and increase the output displacement resolution. Closed-form analytical models of the minification ratio and stiffness of the amplification mechanism were derived. The validity of the models was verified by FEA simulation and testing results. The amplification mechanism and derived analytical models have general applicability to other MEMS transducer designs. The integrated on-chip capacitive displacement sensor and the high linearity of the amplification mechanism are capable of providing precise position feedback, and closed-loop nanopositioning was experimentally demonstrated. The MEMS nanomanipulators provide a small-sized, high-precision, low-cost platform for closed-loop manipulation of nanometer-sized objects.

References

- [1] Scire F E and Teague E C 1978 Piezodriven $50 \mu\text{m}$ range stage with subnanometer resolution *Rev. Sci. Instrum.* **49** 1735–40
- [2] Ku S S, Pinsopon U, Cetinkunt S and Nakajima S 2000 Design, fabrication, and real-time neural network control of a three-degrees-of-freedom nanopositioner *IEEE/ASME Trans. Mechatron.* **5** 273–80
- [3] Ru C H and Sun L N 2005 Improving positioning accuracy of piezoelectric actuators by feedforward hysteresis compensation based on a new mathematical model *Rev. Sci. Instrum.* **9** 095111
- [4] Shen S C, Pan C T and Chou H P 2002 Electromagnetic optical switch for optical network communication *J. Magn. Magn. Mater.* **239** 610–3
- [5] Li F, Wu M C, Choquette K D and Crawford M H 1997 Self-assembled microactuated XYZ stages for optical scanning and alignment *Int. Conf. on Solid-State Sensors and Actuators (Chicago)* pp 319–22
- [6] Cheung P and Horowitz R 1996 Design, fabrication, position sensing, and control of an electrostatically-driven polysilicon microactuator *IEEE Trans. Magn.* **32** 122–8
- [7] Horsley D A, Wongkomet N, Horowitz R and Pisano A P 1999 Precision positioning using a microfabricated electrostatic actuator *IEEE Trans. Magn.* **35** 993–9
- [8] Fukuta Y, Collard D, Akiyama T, Yang E H and Fujita H 1997 Microactuated self-assembling of 3D polysilicon structures with reshaping technology *IEEE Int. Conf. on MEMS* pp 477–81
- [9] Agarwal M, Dutton D T, Theil J A, Bai Q, Par E and Hoen S 2006 Characterization of a dipole surface drive actuator with large travel and force *J. Microelectromech. Syst.* **15** 1726–34
- [10] Hubbard N B and Howell L L 2005 Design and characterization of a dual-stage, thermally actuated nanopositioner *J. Micromech. Microeng.* **15** 1482–93
- [11] Choi S B, Han S S and Lee Y S 2005 Fine motion control of a moving stage using a piezoactuator associated with a displacement amplifier *Smart Mater. Struct.* **14** 222–30
- [12] Chu C L and Fan S H 2006 A novel long-travel piezoelectric-driven linear nanopositioning stage *Precis. Eng.* **30** 85–95
- [13] Millet O, Bernardoni P, Regnier S, Bidaud P, Tsitsiris E, Collard D and Buchailot L 2004 Electrostatic actuated micro gripper using an amplification mechanism *Sensors Actuators A* **114** 371–8
- [14] Lin L W, Pisano A P and Howe R T 1997 A micro strain gauge with mechanical amplifier *J. Microelectromech. Syst.* **6** 313–21
- [15] Chu L L and Gianchandani Y B 2003 A micromachined 2D positioner with electrothermal actuation and sub-nanometer capacitive sensing *J. Micromech. Microeng.* **13** 279–85
- [16] Su X P S and Yang H S 2001 Design of compliant microlverage mechanisms *Sensors Actuators A* **87** 146–56

- [17] Ma H W, Yao S M, Wang L Q and Zhong Z 2006 Analysis of the displacement amplification ratio of bridge-type flexure hinge *Sensors Actuators A* **132** 730–6
- [18] Howell L L 2001 *Compliant Mechanisms* (New York: Wiley)
- [19] Paros J M and Weisbord L 1965 How to design flexure hinges *Mach. Des.* **27** 151–6
- [20] Ugural A C and Fenster S K 2003 *Advanced Strength and Applied Elasticity* (Englewood Cliffs, NJ: Prentice-Hall)
- [21] Petersen K E 1982 Silicon as a mechanical material *Proc. IEEE* **70** 420–57
- [22] Pan B, Xie H M, Xu B Q and Dai F L 2006 Performance of sub-pixel registration algorithms in digital image correlation *Meas. Sci. Technol.* **17** 1615–21
- [23] Sun Y, Fry S N, Potassek D P, Bell D J and Nelon B J 2005 Characterizing fruit fly flight behavior using a microforce sensor with a new comb drive configuration *IEEE/ASME J. MEMS* **14** 4–11
- [24] Gabrielson T B 1993 Mechanical-thermal noise in micromachined acoustic and vibration sensors *IEEE Trans. Electron Devices* **40** 903–9